Journal of Physics and Chemistry of Solids 112 (2018) 270–279

Contents lists available at ScienceDirect

Journal of Physics and Chemistry of Solids

journal homepage: www.elsevier.com/locate/jpcs

Synthesis and characterization of carbon coated $LiCo_{1/3}Ni_{1/3}Mn_{1/3}O_2$ and bio-mass derived graphene like porous carbon electrodes for aqueous Li-ion hybrid supercapacitor

B. Ramkumar [a,b], S. Yuvaraj [a], S. Surendran [a], K. Pandi [a], Hari Vignesh Ramasamy [b], Y.S. Lee [b,**], R. Kalai Selvan [a,*]

[a] Energy Storage and Conversion Devices Laboratory, Department of Physics, Bharathiar University, Coimbatore, 641 046, India
[b] Faculty of Applied Chemical Engineering, Chonnam National University, Gwangju 500-757, Republic of Korea

ARTICLE INFO

Keywords:
Li-hybrid supercapacitor
Porous carbon
Bio-mass
Layered metal oxide
Specific capacity

ABSTRACT

For the fabrication of aqueous Li-ion hybrid supercapacitor, carbon coated $LiCo_{1/3}Ni_{1/3}Mn_{1/3}O_2$ (or $LiCo_{1/3}Ni_{1/3}Mn_{1/3}O_2$@C composite) is synthesized by polymeric precursor method with subsequent thermal decomposition procedures for carbon coating. Graphene like porous carbon is obtained by chemical activation from the biomass of *Agave Americana*. The XRD analysis reveals that $LiCo_{1/3}Ni_{1/3}Mn_{1/3}O_2$ is having a hexagonal layered structure and activated carbon exists in both amorphous and graphitic nature. The TEM image infers that $LiCo_{1/3}Ni_{1/3}Mn_{1/3}O_2$ particles having the non-uniform shape with sub-micron size and the $LiCo_{1/3}Ni_{1/3}Mn_{1/3}O_2$ particles are embedded into amorphous carbon cloud in the composite. The activated carbon shows the specific surface area of 1219 m^2 g^{-1}. Finally, the fabricated aqueous $LiCo_{1/3}Ni_{1/3}Mn_{1/3}O_2$@C||AC hybrid supercapacitor delivers the specific capacitance of 56 F g^{-1} with good capacity retention even after 5000 cycles.

1. Introduction

In the current scenario, the usage of transport vehicles considerably increased, which emits greenhouse gases that lead to global warming. It can be overcome by using eco-friendly energy storage devices that having high energy and high power density in electric vehicles and hybrid electric vehicles [1]. Normally, supercapacitor are used as backup power supply for electronic devices and electric vehicles, as it exhibits long cycle life, high power density than batteries and high energy density than conventional capacitors. Based on the charge storage mechanism and types of electrode, the super capacitors are classified into three types, namely, electric double layer capacitors (EDLCs), pseudocapacitor and hybrid supercapacitor (HSC). In EDLCs, the charges are stored through adsorption of ions on the surface of the electrode material and it posses high power density and long cycle life due to the absence of chemical reactions [2]. In pseudocapacitor, the charge storage mechanism is based on redox reaction that posses high energy density than EDLC [3]. Conversely, hybrid supercapacitor combines the working principle of both EDLC and pseudocapacitor, to achieve high energy density, long potential window, and high-cycle life [4,5]. These outstanding properties of hybrid supercapacitor make it a promising next generation energy storage device. However, a suitable negative and positive electrode material is necessary for HSC cell to avoid the imbalance in reaction kinetics of both electrodes [6].

In this perspective, various metal oxides including $Li_3V_2(PO_4)_3$ [7], LiV_3O_8 [8], TiP_2O_7 [9], $LiTi_2(PO_4)_3$ [9], $LiNiPO_4$ [10], TiO_2 [11], $LiFePO_4$ [12],etc., have been tried as the possible positive electrode material for Li-ion hybrid capacitors. Among these, some of the lithium containing metal oxides provided high energy density of 19.2 Wh kg^{-1} ($LiCoO_2$||GO) [13], 35 Wh kg^{-1} ($LiMn_2O_4$||AC) [14], 40 Wh kg^{-1} ($Li_4Ti_5O_{12}$||$LiCoO_2$) [15]. But, their commercial applications are restricted due to high cost and toxic nature of Co element [16]. As well as, during charge/discharge, the crystal structure of $LiMn_2O_4$ has been changed due to John-Teller distortion [17]. Similarly, preparation of single phase $LiNiO_2$ is difficult, since the nickel ions preferably occupied the position of Li site that blocks the Li ion diffusion pathway and also it is thermally unstable.

Therefore, the mixed transition metal oxide of $LiCo_{1/3}Ni_{1/3}Mn_{1/3}O_2$ is chosen as the positive electrode for Li-ion HSC cell for the present study. These ternary metal combinations has several advantages like rate

* Corresponding author.
** Corresponding author.
E-mail addresses: leeys@chonnam.ac.kr (Y.S. Lee), selvankram@buc.edu.in (R. Kalai Selvan).

https://doi.org/10.1016/j.jpcs.2017.09.012
Received 21 June 2017; Received in revised form 5 September 2017; Accepted 10 September 2017
Available online 12 September 2017

performance due to $LiCoO_2$, high capacity due to $LiNiO_2$ and Mn^{4+} ion facilitates the structural stability [18]. In this structure electrochemical performance is mainly depends on nickel ion because cobalt ion only active at higher voltage range and manganese ion didn't involved in the redox reaction but it was helped to stabilize the crystal structure [19]. $LiCo_{1/3}Ni_{1/3}Mn_{1/3}O_2$ electrode material possesses high capacity and good cycle life associated with the unique electronic structure (Co^{3+}, Ni^{2+} and Mn^{4+}), negligible volume change and high exothermic reaction compare to $LiCoO_2$ [20]. However, the scarce amount of work has been reported on $LiCo_{1/3}Ni_{1/3}Mn_{1/3}O_2$ based hybrid capacitors. $LiCo_{1/3}Ni_{1/3}Mn_{1/3}O_2$||AC hybrid cell provided an initial specific capacitance of 298 F g^{-1} at 100 mA g^{-1}, but it decreased to 240 F g^{-1} after 1000 cycles [21]. Similarly, the $LiCo_{1/3}Ni_{1/3}Mn_{1/3}O_2$||AC delivered the specific capacity of 25 mAh g^{-1} at 6 mA cm^{-2} and 10 mAh g^{-1} at 20 mA cm^{-2} [22]. Nevertheless, it has some drawbacks like capacity fading, poor cycle life and rate capability, which is due to the phase transitions and formation of unstable surface interface layer resulting in unwanted side reactions [23].

Carbon coating or impregnation of active materials into the amorphous carbon cloud is the possible way to mitigate the some of the above said problems [24]. Normally, this carbon layer/cloud suppresses the electrode side reaction by avoiding contact between active material and electrolyte solution, and act as a buffer to accommodate volume strain during lithiation/de-lithiation for stable cycle life [25]. It also acts as a barrier to reduce the aggregation of electrode active particles and increase the stability of the crystal structure.

On the other hand identifying the suitable negative electrode is also mandatory. Among the carbonaceous materials, activated carbon (AC) is considered as one of the best candidate for negative electrode because of its peculiar properties like good chemical stability in different pH condition, amphoteric behaviour, wide operating temperature [26] and high surface area (porous nature) [27], good conductivity, thermal stability, and cost effective [28]. Biomass is one of the important sources for the preparations of AC, since it is cost effective for large scale production, easily renewable and wide availability and accessibility as well as it provides more oxygen functional groups [29]. It is well known that the physiochemical properties (pore structure and surface functional groups) of AC are mainly dependent on the nature of the precursor material and method of preparation (activating agent, temperature and time) [29,30]. In this line, *Agave Americana* is chosen as the biomass for the preparation of AC since naturally it contains more fiber, components of fiber-yielding crop and more abundant in nature. As well as it contains 68–80% of cellulose that favour for getting more activated carbon. It is “zero waste” plant to use activated carbon and the fibers properties are low density, high tenacity and high moisture absorbency [31].

Here, the positive electrode of $LiCo_{1/3}Ni_{1/3}Mn_{1/3}O_2$ is synthesized through simple polymeric precursor method and carbon coated $LiCo_{1/3}Ni_{1/3}Mn_{1/3}O_2$ is achieved by thermal decomposition method using glucose as a carbon source. The *Agave Americana* is used for the preparation of AC negative electrode. The electrochemical performance of prepared $LiCo_{1/3}Ni_{1/3}Mn_{1/3}O_2$, carbon coated $LiCo_{1/3}Ni_{1/3}Mn_{1/3}O$ and AC is analysed through CV and GCD in 0.5 M Li_2SO_4 electrolyte using 3 electrode systems. Finally, aqueous Li ion hybrid supercapacitor is fabricated using carbon coated $LiCo_{1/3}Ni_{1/3}Mn_{1/3}O_2$ with AC and studied its electrochemical performances. The fabricated device delivers the energy density of 20 Wh kg^{-1} and power density of 264 W kg^{-1}.

2. Experimental methods

2.1. Synthesis of $LiCo_{1/3}Ni_{1/3}Mn_{1/3}O_2$ and $LiCo_{1/3}Ni_{1/3}Mn_{1/3}O_2$@C composite

$LiCo_{1/3}Ni_{1/3}Mn_{1/3}O_2$ was prepared by a polymeric precursor method using citric acid as a chelating agent and polyethylene glycol as a polyesterification agent. The starting precursors utilized in the preparation process were lithium nitrate ($Li(NO_3)_2$), nickel nitrate ($(Ni(NO_3)_2.6H_2O$), manganese nitrate ($Mn(NO_3)_2{\cdot}4H_2O$) and cobalt nitrate ($Co(NO_3)_2.6H_2O$). Initially, citric acid was dissolved into distilled water and converted into citrate aqueous solution. Similarly, the cationic precursors were dissolved in desired amount of double distilled water and mixed with citrate solution under magnetic stirring. The metal cation to citric acid molar ratio was kept as 2:1 M ratio. Subsequently, the desired amount of polyethylene glycol was added in to the above mixture and dried at 80 °C for inducing the metal-citrate polymerization process. After a few hours, it produces a transparent polymeric resin due to the slow evaporation of water molecules. Finally, an exothermic reaction takes place by the way of polymeric resin pre-heated at the 300 °C for 1 h under air atmosphere. The preheated sample was ground well and subsequently calcinated at 900 °C for 10 h to attain a phase pure formation of $LiCo_{1/3}Ni_{1/3}Mn_{1/3}O_2$.

For the preparation of carbon coated $LiCo_{1/3}Ni_{1/3}Mn_{1/3}O_2$, the prepared $LiCo_{1/3}Ni_{1/3}Mn_{1/3}O_2$ was mixed with glucose and 5 ml of ethanol and ground few hours to obtain a homogeneous mixture. Here, glucose was used as the carbon source. Subsequently, the mixture was carbonized at 600 °C for 3 h under N_2 atmosphere and obtained the carbon coated $LiCo_{1/3}Ni_{1/3}Mn_{1/3}O_2$ particles.

2.2. Preparation of activated carbon from biomass

The graphene like porous carbon was prepared using a biomass *Agave Americana*. Initially, the precursor was cut into tiny pieces and cleaned with double distilled water. Subsequently, it dried under daylight and preheated at 200 °C for 12 h to remove the moisture content present in it. After that, 20 g of the preheated sample and 10 g of KOH crystals were well mixed in the mass ratio of 2:1 in 100 ml of double distilled water and kept for 43 h. Then, the mixture was placed inside the furnace at 100 °C for 12 h and further carbonized at 700 °C for 3 h under argon atmosphere. Subsequently, the carbonized sample was thoroughly washed with pure water along with desired amount of HCl to remove the impurities present in the sample. Finally, the washed sample was dried at 80 °C for 12 h and obtained the porous carbon.

2.3. Electrode preparation and hybrid cell fabrication

The $LiCo_{1/3}Mn_{1/3}Ni_{1/3}O_2$ electrodes were made by mixing 75% of active material, 15% of carbon black as conductive additive and 10% of PVdF as a binder in 0.3 ml of N-methyl 2-pyrrolidine to obtain a homogeneous slurry. The slurry (13.5 μl) was coated on the stainless steel (1×1 cm^2) substrate and dried at 80 °C overnight in a vacuum oven. The calculated mass of the active material loading was 1 mg. The same procedure was adopted to prepare AC electrode. The electrochemical performance of both electrodes was analysed using cyclic voltammogram (CV) and galvanostatic charge/discharge analysis.

Further, the aqueous Li-ion hybrid supercapacitor was constructed following procedure. Initially, the positive & negative electrodes, along with membrane were soaked into the electrolyte. Then, two electrodes were placed one above the other and a polypropylene sheet was sandwiched in between the electrodes. Here, the polypropylene sheet was served as a separator and electrolyte contained. Finally, this architecture was placed within the electrolyte solution and investigated for their electrochemical performance.

2.4. Characterization techniques and instrument details

The crystallinity and phase purity of the $LiCo_{1/3}Mn_{1/3}Ni_{1/3}O_2$ and AC were studied by Powder XRD using X'Pert PRO PANalytical X-ray Diffractometer. The surface area, pore size and pore distribution of the AC was carried out using nitrogen adsorption-desorption experiments at 77 K (Micromeritics ASAP 2010 surface area analyzer). The Bruker tensor 27 model was used for the FT-IR analysis in the range of 400–4000 cm^{-1}. Raman spectra of the prepared sample were recorded using a lab Raman dispersive spectrometer (Lab Ram HR 800, Horiba, Japan). The

morphological features were studied using high-resolution transmission electron microscopy (JEOL 2100 F at 200 KV). The microscopic porous structure of the AC was observed via scanning electron microscopy (SEM) (Quanta 200 ESEM, FEI, USA). The Bio-Logic SP 150 was used to analyze the electrochemical performances of the electrodes and Ag/AgCl and Pt wire were used as a reference and counter electrode for three electrode system.

3. Results and discussion

3.1. Characterization of $LiCo_{1/3}Ni_{1/3}Mn_{1/3}O_2$ and $LiCo_{1/3}Ni_{1/3}Mn_{1/3}O_2$@C composite

3.1.1. Structural and morphological analysis

Fig. 1(a) shows the XRD pattern of $LiCo_{1/3}Ni_{1/3}Mn_{1/3}O_2$ with high intense diffraction peaks which inferred the good crystallinity of $LiCo_{1/3}Ni_{1/3}Mn_{1/3}O_2$. It has a hexagonal structure belonging to the *R3m* space group of a hexagonal α-$NaFeO_2$ structure. The lattice is formed by oxygen atoms in ABC stacking with alternating layers containing mixtures of nickel, cobalt and manganese atoms [32]. The well-resolved (006)/(102) and (108)/(110) doublets in the XRD patterns of the prepared powders indicate that the compound exist in well-aligned layered structure [33]. It is well known that the layered structure is the favorable one for Li-ion intercalation/de-intercalation process and paves the way for easiest diffusion of lithium ions into or from the electrode material. No other individual metal oxide peaks are observed that reveals the phase pure formation of $LiCo_{1/3}Ni_{1/3}Mn_{1/3}O_2$. The calculated lattice parameter values are, a = 2.869 Å and c = 14.106 Å. The calculated c/a ratio and cell volume are 4.91 and 100.56 $Å^3$, respectively. These calculated structural parameters are well matched with the previous reports [18,33,34]. Further, using Scherrer equation the calculated crystallite size is 37 nm. Fig. 1(b) shows the FT-IR spectrum of prepared $LiCo_{1/3}Ni_{1/3}Mn_{1/3}O_2$ and it shows the two bands at 535 and 595 cm^{-1} corresponds to M-O stretching and O-*M*-O bending vibration mode (M = Ni, Co, Mn) of MO_6 octahedra in the $LiCo_{1/3}Ni_{1/3}Mn_{1/3}O_2$ system [35,36]. In addition, the observed less intense shoulders in between 420 and 450 cm^{-1} attributed to the bonding of Li^+ ions with O^{2-} ions in LiO_6 octahedra [36]. Overall, FT-IR spectrum reveals the characteristic bands of $LiCo_{1/3}Ni_{1/3}Mn_{1/3}O_2$ related to the position of MO_6 and LiO_6 octahedra. The FT-IR spectrum of carbon coated $LiCo_{1/3}Ni_{1/3}Mn_{1/3}O_2$ shows the absorption band at 1630 cm^{-1} and 1745 cm^{-1} corresponding to C═O and C═C band. It reveals the presence of carbon residue in the $LiCo_{1/3}Ni_{1/3}Mn_{1/3}O_2$ [37].

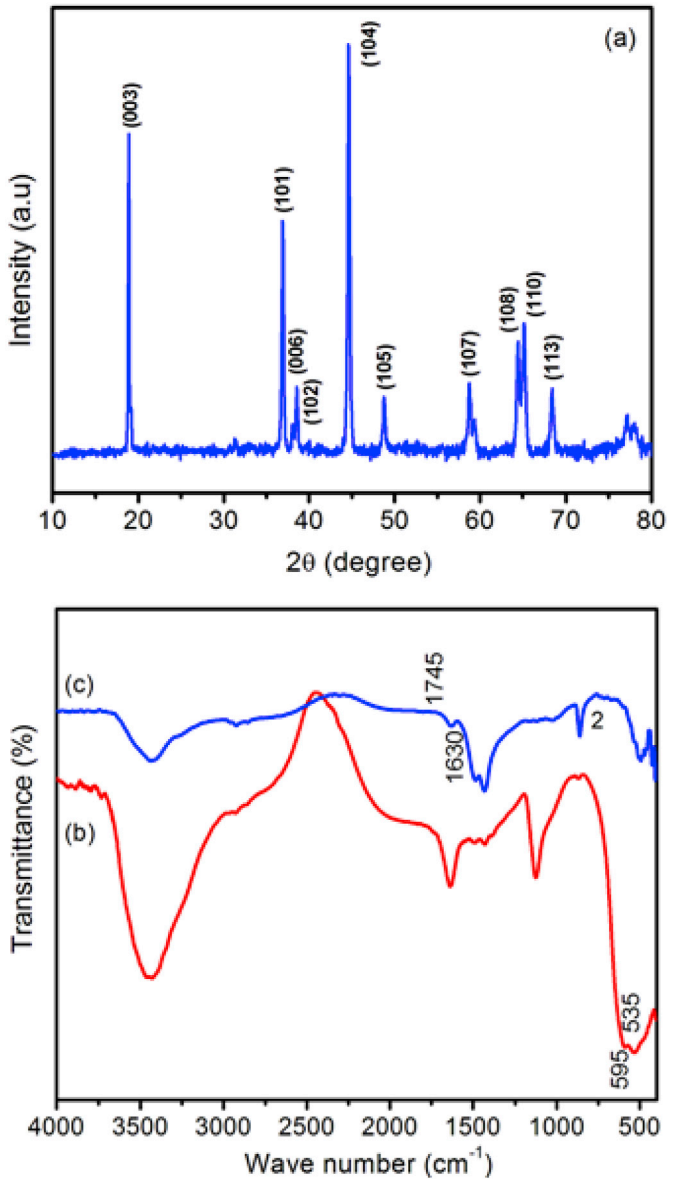

Fig. 1. (a) XRD pattern of $LiCo_{1/3}Ni_{1/3}Mn_{1/3}O_2$, FT-IR spectra of (b) $LiCo_{1/3}Ni_{1/3}Mn_{1/3}O_2$ and (c) carbon coated $LiCo_{1/3}Ni_{1/3}Mn_{1/3}O_2$.

The TEM images of $LiCo_{1/3}Mn_{1/3}Ni_{1/3}O_2$ particles are shown in Fig. 2(a). It shows the non-uniform shaped particles in the size range of 0.5–0.8 μm. The HRTEM image (Fig. 2(b)) shows well aligned lattice fringes confirming the highly crystalline nature of $LiCo_{1/3}Mn_{1/3}Ni_{1/3}O_2$. The calculated d-spacing is 0.19 nm, which corresponds to the (104) plane of $LiCo_{1/3}Mn_{1/3}Ni_{1/3}O_2$. Fig. 2(c) shows the selected area electron diffraction (SAED) pattern that indicates the high intense dot pattern with high symmetry. It further reveals the high crystalline nature as well as long range order of $LiCo_{1/3}Mn_{1/3}Ni_{1/3}O_2$. The measured d-spacing values are 0.254, 0.219, 0.196, 0.244, 0.479 and 0.259 nm, which are merely coincided with the lattice planes of (102), (004), (105), (101), (003) and (006), respectively. This result further confirms the hexagonal structure of $LiCo_{1/3}Ni_{1/3}Mn_{1/3}O_2$.

Fig. 2(d and e) shows the low magnification TEM image of the carbon coated $LiCo_{1/3}Ni_{1/3}Mn_{1/3}O_2$. It can be seen that $LiCo_{1/3}Ni_{1/3}Mn_{1/3}O_2$ particles are embedded into the amorphous carbon matrix. This carbon matrix modified the surface chemistry of the electrodes and it could act as a protective layer which increases the structural stability, reduces the phase transition and suppresses the dissolution of $LiCo_{1/3}Ni_{1/3}Mn_{1/3}O_2$ [38]. Fig. 2(f) shows the HRTEM image of carbon coated $LiCo_{1/3}Ni_{1/3}Mn_{1/3}O_2$. The well defined amorphous layer on the surface of the $LiCo_{1/3}Ni_{1/3}Mn_{1/3}O_2$ is clearly revealed the coating of carbon through the thermal decomposition of glucose [39]. The measured inter plane spacing (d) is about 0.187 nm, which corresponds to the (104) of $LiCo_{1/3}Ni_{1/3}Mn_{1/3}O_2$.

3.1.2. Electrochemical analysis of $LiCo_{1/3}Mn_{1/3}Ni_{1/3}O_2$ using half cell

The electrochemical performance is analysed using CV and GCD analysis. Importantly, the electrochemical performance of the electrode material mainly influenced by different factors including, active species, surface area, pore size and volume, morphology, hydration sphere radius of electrolyte (cations/anions) ions, and pH of the electrolyte [20,40–44]. Among the aforementioned key factors, the pH of the electrolyte is very essential factor. In order to identify the effect of pH, the $LiCo_{1/3}Mn_{1/3}Ni_{1/3}O_2$ electrode is examined in 0.5 M Li_2SO_4 electrolyte at various pH conditions through CV analysis in the potential range of 0–0.6 V *vs* Ag/AgCl. Fig. 3(a) shows the CV curve of $LiCo_{1/3}Mn_{1/3}Ni_{1/3}O_2$ electrode at 0.2 mV s^{-1} measured in different pH conditions (pH 9 to pH 14). The CV curve clearly demonstrates that oxidation peak is increased while increasing the pH of the electrolyte solution. At low pH, more number of H^+ ions is intercalated into the layered structure that occupies the Li^+ ion site and it cannot be de-intercalated from the structure [45]. So the H^+ ion inhibits the intercalation of Li^+ ion during the discharging

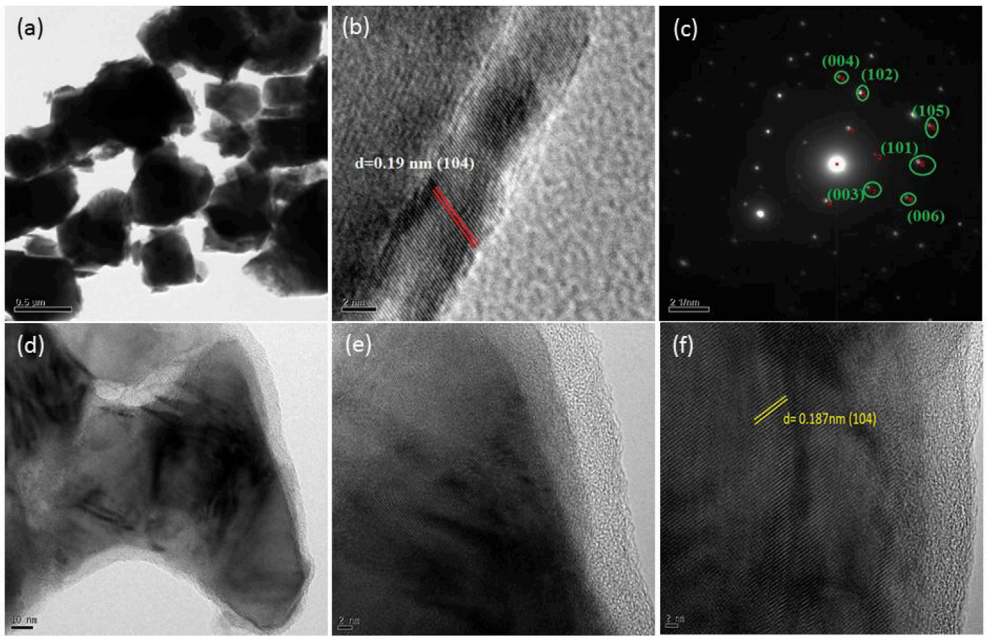

Fig. 2. (a) TEM image, (b) HRTEM image and (c) SAED pattern of $LiCo_{1/3}Ni_{1/3}Mn_{1/3}O_2$, (d) & (e) TEM image and (f) HRTEM image of carbon coated $LiCo_{1/3}Ni_{1/3}Mn_{1/3}O_2$.

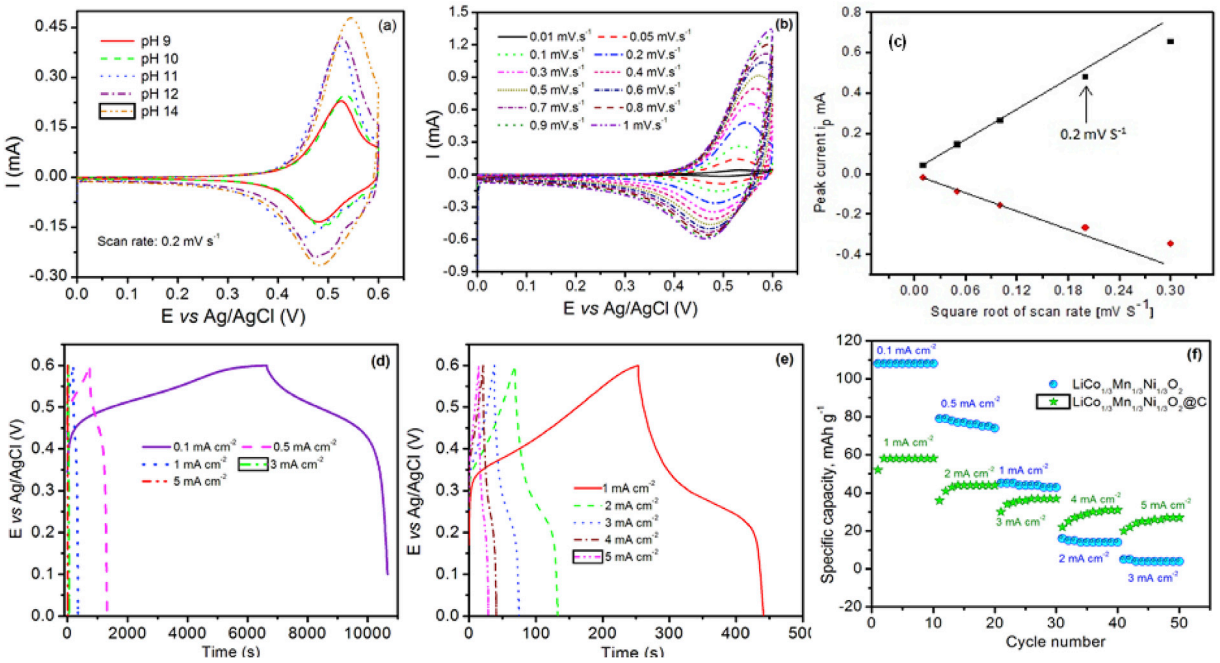

Fig. 3. (a) CV curve of $LiCo_{1/3}Mn_{1/3}Ni_{1/3}O_2$ at different pH conditions (b) CV curve at different scan rates of $LiCo_{1/3}Mn_{1/3}Ni_{1/3}O_2$, (c) peak peak current (i_p) *vs* square root of scan rate ($\upsilon^{1/2}$) of $LiCo_{1/3}Mn_{1/3}Ni_{1/3}O_2$, GCD curve of (d) $LiCo_{1/3}Mn_{1/3}Ni_{1/3}O_2$ and (e) carbon coated $LiCo_{1/3}Mn_{1/3}Ni_{1/3}O_2$ composite at different current densities, and (f) cycling stability curve of $LiCo_{1/3}Mn_{1/3}Ni_{1/3}O_2$ and carbon coated $LiCo_{1/3}Mn_{1/3}Ni_{1/3}O_2$.

process that reduces the capacitance. Also, H^+ ions are less volume than other cations and are chemically more active, easily covalently bonded with oxygen atom which give rise to large electrode polarization subsequently degrades the capacitance [45]. On the other hand, increasing the pH of the electrolyte reduces the concentration of H^+ ions and simultaneously it increases the Li^+ ions intercalation as well as increases the oxidation peak current [46]. Overall, the CV curve reveals that the $LiCo_{1/3}Mn_{1/3}Ni_{1/3}O_2$ provides the good electrochemical performances at pH 14. Therefore, the preceding studies are carried out in pH 14.

Fig. 3(b) shows the CV curve of $LiCo_{1/3}Mn_{1/3}Ni_{1/3}O_2$ in 0.5 M Li_2SO_4 electrolyte solution at different scan rates between 0 and 0.6 V (*vs* Ag/AgCl). It can be seen that two different regions are noticed in the CV curve such as potential independent (0–0.35 V *vs* Ag/AgCl and 0.55–0.6 V *vs* Ag/AgCl) and potential dependent (0.35–0.55 V *vs* Ag/AgCl) variation of current regions. The potential independent current regions infer the electric double layer charge storage mechanism of the electrode and the potential dependent current region infers that the electrode stores the charge based on faradaic reaction mechanism. The CV curve clearly witnessed that the electrode stores the maximum amount of charge based on faradaic reaction rather than EDL capacitive. Here, the faradaic reaction mechanism arises from the intercalation/de-intercalation mechanism rather than the surface redox mechanism [20].

The plausible electrochemical reaction mechanism of $LiCo_{1/3}Mn_{1/3}Ni_{1/3}O_2$ electrode can be expressed in the following manner.

During charging process (de-intercalation)

$$LiCo_{1/3}Ni_{1/3}Mn_{1/3}O_2 \rightarrow Li_{1-x}Co_{1/3}Ni_{1/3}Mn_{1/3}O_2 + xLi^+ + xe^- \quad (1)$$

During discharging process (Intercalation).

$$Li_{1-x}Co_{1/3}Ni_{1/3}Mn_{1/3}O + xLi^+ + xe^- \rightarrow LiCo_{1/3}Ni_{1/3}Mn_{1/3}O_2 \quad (2)$$

In the electrochemical reaction, Ni^{2+}/Ni^{3+} ions participating the oxidation/reduction reaction because the activation energy of Ni^{2+} ion is less than 0.6 V *vs* Ag/AgCl [46]. But, the activation energy of other two metal ions (Mn^{3+}/Mn^{4+} and Co^{2+}/Co^{3+}) is above 0.6 V *vs* Ag/AgCl [47,48]. The calculated specific capacitance is 411 F g^{-1} at 0.2 mV s^{-1}. The high specific capacitance is mainly arises from the well aligned layered structure, lower cation disorders, less probability of other cations occupying the Li^+ ion site, and easy de-intercalation/intercalation of Li^+ ions [19].

Similarly, the feeble peak potential difference is observed in between the oxidation and reduction peaks of $LiCo_{1/3}Mn_{1/3}Ni_{1/3}O_2$ at different scan rates (Fig. 3(b)), which reveals the fast-faradaic reaction and good electrochemical reversibility of the active material. As well as the anodic peak current increased with increasing in scan rate, that evidences the scan rate dependence of peak current [49]. The calculated specific capacitances are 588, 485, 452, 411, 372, 333, 299, 267, 243, 223, 204 and 188 F g^{-1} for the corresponding scan rate of 0.01, 0.05, 0.1, 0.2, 0.3, 0.4, 0.5, 0.6, 0.7, 0.8, 0.9 and 1 mV s^{-1}, respectively. The $LiCo_{1/3}Mn_{1/3}Ni_{1/3}O_2$ electrode is still retaining the well-defined shape even at high scan rate of 1 mV s^{-1}. It indicates that the active material charged and discharged at faster rate [50]. Unfortunately, the oxidation and reduction peaks are shifted towards positive and negative side respectively, and peaks get slightly broadened. It reveals that the slight increase of electrode resistance, it is obvious in nature [51,52]. Here, two observations derived from CV profiles with different scan rates. First, the potential difference between cathodic and anodic peak is less than 58 mV. Secondly, the peak current is proportional to the square root of the scan rate, based on a diffusion-controlled process. The scan rate profile elucidates that $LiCo_{1/3}Mn_{1/3}Ni_{1/3}O_2$ is a good reversible electrochemical system which satisfy the minimum two condition of the reversible system [53]. A plot of normalized peak current with square root of scan rates ($\upsilon^{1/2}$) (Fig. 3(c)) shows two different regions, *i.e.,* a linear relation occurred below 0.2 mV s^{-1} and above it obeys the non-linear relation. This suggests that the $LiCo_{1/3}Mn_{1/3}Ni_{1/3}O_2$ electrode maintains the reversibility up to a critical scan rate of 0.2 mV s^{-1} at room temperature [53]. The diffusion coefficient is one of the important factors to analyze the electrode kinetics and rate determining step during intercalation process which is measured using peak current versus square root of scan rate ($\upsilon^{1/2}$) plot. The diffusion coefficient is calculated using Randles-Sevick eqn. (3) [54,55],

$$I_p = 0.4463\ n^{3/2}\ F^{3/2}\ C_o\ A\ R^{-1/2}\ T^{-1/2}\ D_{Li}^{1/2}\ v^{1/2} \quad (3)$$

Where, n is the number of electrons transferred during the electrochemical reaction, F is the Faraday constant (96486 C), C_o is the molar concentration of Li^+ ion (mol cm^{-3}), A is the area of the electrode (cm^2), R is the gas constant (8.314 J mol^{-1} K^{-1}), T is the absolute temperature (K) and D is the diffusion coefficient (cm^2 s^{-1}). The calculated diffusion coefficient of $LiCo_{1/3}Mn_{1/3}Ni_{1/3}O_2$ is 6.0436×10^{-10} cm^2 s^{-1}.

Fig. 3(d) shows the GCD curve of $LiCo_{1/3}Ni_{1/3}Mn_{1/3}O_2$ at different current densities. The GCD curves also clearly evidences the coexistence of both faradaic and EDL capacitive charge storage mechanism of the electrode material. It can be seen that the discharge time is decreases with increase in current density. As it is known, the discharge time is directly proportional to the specific capacitance of the electrode material [56]. In this regard, the calculated discharge specific capacity is 108, 79, 45, 16, and 5 mAh g^{-1} at current densities of 0.1, 0.5, 1, 2 and 3 mA cm^{-2}. At high current densities, ionic motion within the electrode/electrolyte interface is too slow for the charge distribution to reach the equilibrium at high current density thus leads to reduce the specific capacity [57,58]. Fig. 3(e) shows the GCD curve of $LiCo_{1/3}Ni_{1/3}Mn_{1/3}O_2$@C composite at different current densities. It can be clearly seen that discharge time is high, when compared with pristine $LiCo_{1/3}Ni_{1/3}Mn_{1/3}O_2$ at all current densities. The calculated specific capacity is 52, 36, 30, 22 and 20 mAh g^{-1} corresponds to the high current densities of 1, 2, 3, 4 and 5 mA cm^{-2}. The rate capability curve of $LiCo_{1/3}Ni_{1/3}Mn_{1/3}O_2$ is shown in Fig. 3(f). The $LiCo_{1/3}Mn_{1/3}Ni_{1/3}O_2$ electrode shows the superior rate capability even at high current density, but the specific capacitance is decreased at high current density. On the other hand, carbon coated $LiCo_{1/3}Ni_{1/3}Mn_{1/3}O_2$ (Fig. 3(f)) electrode shows the high specific capacity even at high current density and also it increases with further cycling. The reason for the increasing specific capacitance of is due to activation process [38].

Overall, the amorphous carbon in the carbon coated $LiCo_{1/3}Ni_{1/3}Mn_{1/3}O_2$ can greatly improve the electrochemical performances like cycle life, specific capacitance, with good capacitance retention. The carbon composite providing a good electrical contact between the active material and current collector and facilitate to additional charge storage for ions [59]. In addition, the carbon composite restricts the side reactions of the electrode material during the charge/discharge process, and dissolution of active material in the electrolyte solution [60]. The carbon composite further support to faster lithium ion even at high current rate and also it can reduce the polarization of the electrode material [61]. Further, the carbon composite retains the crystal structure, restricts the volume variation and amorphous phase formation during the electrochemical reaction [61]. Hence, carbon coated $LiCo_{1/3}Ni_{1/3}Mn_{1/3}O_2$ is identified as the suitable positive electrode for the fabrication of Li-ion hybrid cell.

3.2. Physicochemical properties of activated carbon

Fig. 4(a) shows the XRD pattern of biomass derived AC. It shows the broad diffraction peak in the range of 20–30° which corresponds to the (002) plane reflection. It confirmed that AC has turbostatic carbon structure. Also, the weak diffraction peak observed at 44° which corresponds to (100) reflection of honeycomb structure and is formed by sp^2 hybridized carbon [30]. These results are assured that the prepared activated carbon exhibits in both amorphous and graphitic nature. Further, interspacing distance (d) and R-factor calculated from XRD results and are 0.368 nm and 2.59, respectively. The calculated d-spacing is higher than the graphite (0.35 nm), therefore it is believed that this structure makes easy diffusion of lithium ions during charging/discharging process. The number of carbon sheets arranged as single layers in activated carbon can be measured by using the empirical parameter R. The R value is the ratio of the height of the (002) peak and the background (R = B/A). If the R factor is minimum, the sample contains more number of single layered carbons, which can store more number of lithium ions [62]. The calculated R-factor implies that non-parallel arrangement of carbon single layer amorphous carbon that allows more lithium ion intercalation into the structure compared graphitic carbon [63,64].

The FT-IR spectrum AC is given in Fig. 4(b), which shows three strong absorption bands at 1276, 1582 and 3411 cm^{-1} corresponds to the C═O (carbonyl stretching and vibration in quinine and phenols or ester groups) and O—H stretching mode of hydroxyl groups due to adsorption of water molecules [30]. It confirmed the presence of functional groups in the prepared AC. This functional group improves the wettability of the electrode and also provides additional pseudocapacitance to the electrode. Fig. 4(c) shows the Raman spectrum of activated carbon. It shows two broad peaks at 1580 and 1330 cm^{-1} is corresponds to G-band (graphitic carbon) and D-band (disorder carbon) respectively. The disordered aromatic carbon structure is arisen due to the weak interaction between the adjacent layers in the graphitic lattice. Moreover, the ordered aromatic carbon structure is due to strong C—C bonding within

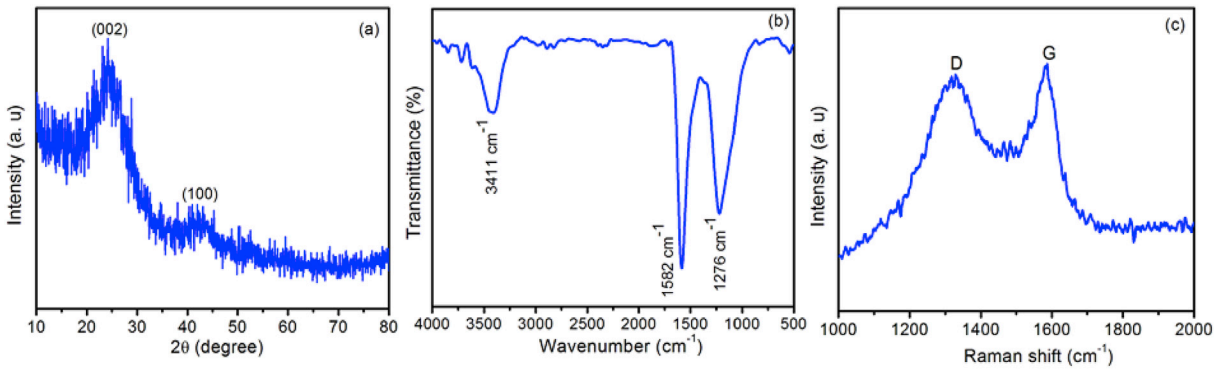

Fig. 4. (a) XRD pattern, (b) FT-IR spectrum, (c) Raman spectrum for Activated Carbon.

the graphite layers [30]. Raman spectrum indicates that high contribution of graphitic carbon present in the sample increases the electronic conductivity. The porous morphology of the prepared AC is analysed by SEM (Fig. 5(a)). It shows that the presence of different kind of pores in the activated carbon. This pore structure is created by the following reasons. The reactions between the precursors and KOH, *i.e.,* the potassium ions intercalate into the lamella of the crystallite. After activation and carbonization process, the potassium ions are removed from a carbon material by leaching of distilled water and finally the lamella cannot return their original state, resulting in the formation of porous structure. This different kinds of pores are interconnected leads to maximum wetting by the electrolyte solution then the maximum surface area of activated carbon involved in the electrochemical performance [65]. Fig. 5(b) shows the TEM image of porous carbon that seems to be a thin layered multifolded graphene like structure. HRTEM image (Fig. 5(c)) clearly displays the lattice planes and the calculated d-spacing value is 0.36 nm, which corresponds to the (002) plane of graphitic carbon. This result assured that the prepared porous carbon prominently exist in graphitic like structure than disordered structure. The observed results well coincided with the Raman results.

Fig. 6(a) shows the N_2 adsorption/desorption curve of prepared AC. A small hysteresis loop is observed for AC that indicates the presence of mixed pores of meso and macroporosity. The hysteresis loop clearly indicates the existence of micropores (2 nm at $P/P_o < 0.5$), mesopores (2–50 nm; P/P_o in between 0.5 and 0.9) and macropores (>50 nm at $P/P_o > 0.9$) [30]. Area of hysteresis loop is attributed to the presence of slit-shaped and ink bottle type pores and maximum amount of mesoporosity in AC. The obtained specific surface area of the prepared activated carbon is 1219 $m^2\ g^{-1}$. Pore size distribution analysed from Barrett-Joyner-Halenda (BJH) method is shown in Fig. 6(b). The obtained high and small peak centered at 3 and 90 nm clearly assures that the prepared AC consists of meso and macropores. The presence of mesopores supports to provide path ways to easy access of electrolyte ions into the electrode material for obtaining high specific capacitance.

The electrochemical performance of AC is carried out in the negative potential window from 0 to −1 V *vs* Ag/AgCl in 0.5 M Li_2SO_4 aqueous electrolyte. Fig. 7(a) shows the CV curve of AC at 0.5 mV s^{-1}. The observed broad hump is may be due to redox reaction of oxygen functional groups in the electrode material [63]. However, the AC is stored the maximum amount of charge based on EDLC capacitive mechanism rather than pseudocapacitive mechanism. The calculated specific capacitance of activated carbon is 236 F g^{-1} in 0.5 M Li_2SO_4 at 0.5 mV s^{-1}. Fig. 7(b) shows the CV curve of ACs at different scan rates. It can be seen that the current area under the CV curve increases with increasing scan rates. The calculated specific capacitances are 249, 239, 236, 235, 236, 232, 231, 229, 227 and 238 F g^{-1} corresponding to 0.1–1 mV s^{-1} in the interval of 0.1 mV s^{-1}. The specific capacitance is linearly decreases with increasing scan rate. It reveals that at low scan rate, the Li^+ ions from electrolyte having sufficient time to adsorb/de-sorb from the electrode, leads to high specific capacitance. However, at high scan rate, the Li^+ ions from electrolyte does not having sufficient time to adsorb/desorbed from the electrode, leads to low specific capacitance. It shows that the AC exhibits excellent specific capacitance retention of 95.58%. In addition, the CV curves clearly evidence the presence of redox peaks even at high scan rate, which indicates that good electrochemical reversibility of oxygen functional groups.

Fig. 7(c) shows the GCDs curve of AC at different current densities. It also evidenced the co-existence of both pseudocapacitive and EDL capacitive mechanism. However, the EDL capacitive mechanism is dominant than pseudocapacitive. It can be seen that the discharge time is decreases with increase of current density, which infers the decrease of specific capacitance. Fig. 7(d) represents the rate capability curve of AC electrode. At first cycle, the AC electrode delivered the specific capacitance of 168 F g^{-1} at 1 mA cm^{-2}. Unfortunately, after 1st cycle the specific capacitance is getting decreased to 164 F g^{-1}, which may be due to ion trapping or surface reaction of the electrode. It can be seen that the activated carbon retains its specific capacitance value for further cycling. Similarly, the electrode delivers the specific capacitance of 148, 126, 120 and 100 F g^{-1} at current densities of 2, 3, 4 and 5 mA cm^{-2}. Subsequently, after 10 cycles, the calculated specific capacitance is 164, 144, 126, 112 and 90 F g^{-1} for respective current densities. It can be observed that there is no drastic loss of specific capacitance which reveals the good

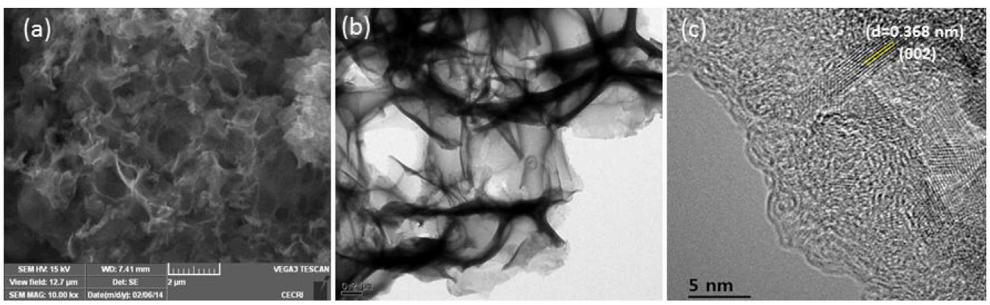

Fig. 5. (a) SEM image (b) TEM and (c) HRTEM image of Activated Carbon.

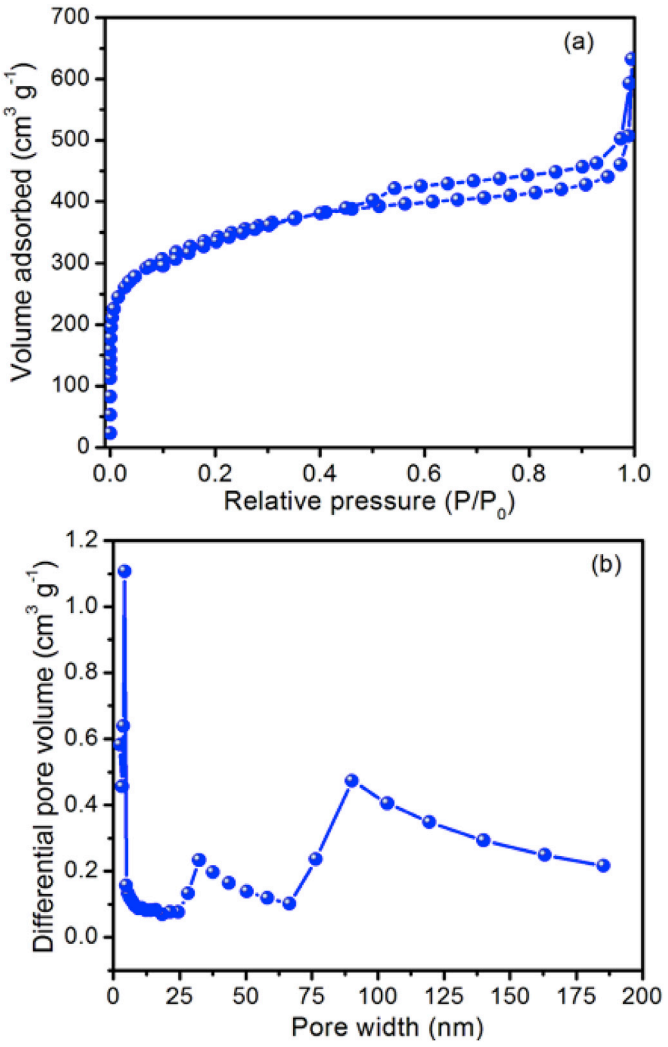

Fig. 6. (a) N_2 adsorption-desorption isotherm, and (b) pore size distribution of AC

electrochemical cycling stability and capacitance retention of the electrode material.

3.3. *Electrochemical performances of $LiCo_{1/3}Ni_{1/3}Mn_{1/3}O_2$@C ||AC hybrid cell*

It is well known that the hybrid supercapacitor has the major advantages including excellent cyclic stability, good specific capacitance, improved energy density and high working potential window than the symmetric supercapacitor. As is known, the mass balancing between the positive and negative electrode is essential to achieve high performance supercapacitor. The mass balancing of the electrodes can be achieved by using the following equation

$$\frac{m_+}{m_-} = \frac{C_- \times \Delta V_-}{C_+ \times \Delta V_+} \quad (4)$$

where, m_+ & m_- is the mass of the positive and negative electrodes, respectively. C_- & C_+ is the specific capacitance contribution of both positive (452 F g^{-1}) and negative (249 F g^{-1}) electrodes, respectively. ΔV_- & ΔV_+ is the working potential of positive (0.6 V) and negative (1 V) electrodes, respectively. Hence, the calculated mass ratio between the electrodes should be 1. The similar procedure was adopted to calculate the mass ratio between $LiCo_{1/3}Mn_{1/3}Ni_{1/3}O_2$ and AC. Subsequently, to optimize the mass ratio between positive and negative electrodes, the device were fabricated at different mass ratios like 0.75:1,1:1,1.25:1,1.5:1, 1.75:1, 2:1 and 2.5:1. In this present case, the electrode masses of AC are fixed and varied the masses of $LiCo_{1/3}Mn_{1/3}Ni_{1/3}O_2$. Fig. 8 (a) shows the GCDs curves of aqueous Li-HSC at different mass ratio. It can be seen that the discharge time of the aqueous Li-HSC decreases with increase of $LiCo_{1/3}Mn_{1/3}Ni_{1/3}O_2$ mass. Surprisingly, the charge/discharge pleatu regions are clearly noticed when increasing $LiCo_{1/3}Mn_{1/3}Ni_{1/3}O_2$ mass. The calculated discharge specific capacitance at different mass ratios are 129 F/g (0.75:1), 112 F/g (1:1), 108 F/g (1.25:1), 87 F/g (1.5:1), 84 F/g (1.75:1), 84 F/g (2:1) and 57 F/g (2.5:1) at 0.1 mA/cm^2 current density. The GCD analysis reveals that the Li-HSC shows the higher specific capacitance while fixing the mass ratio of 0.75:1 ($LiCo_{1/3}Mn_{1/3}Ni_{1/3}O_2$||AC). Therefore, the same ratio is used for the cell fabrication in the subsequent electrochemical analysis.

Fig. 8 (b) shows the CV curve of the fabricated Li-ion hybrid cell using $LiCo_{1/3}Ni_{1/3}Mn_{1/3}O_2$ as the positive electrode and AC as the negative electrode in 0.5 M Li_2SO_4 electrolyte at different scan rate of 1, 5 and 10 mV s^{-1}. The fabricated device can work upto 1.6 V without any O_2 or H_2 evolution. In charging process, the Li-ion is adsorbed on the surface of the AC and then unbalancing force will be created. So, the Li-ion is de-intercalated from $LiCo_{1/3}Mn_{1/3}Ni_{1/3}O_2$. During the discharging process the Li-ion de-adsorbed on the surface of AC and back into the electrolyte solution and Li-ions intercalated into the host structure [59]. The calculated specific capacitance is 51, 30 and 24 F g^{-1} and its corresponding scan rates of 1, 5 and 10 mV s^{-1}. Fig. 8 (c) shows the GCD curve of fabricated Li-ion HSC device using pristine $LiCo_{1/3}Ni_{1/3}Mn_{1/3}O_2$ as positive electrode. It can be seen that the device exhibited the specific capacitance of 90 F g^{-1}. Unfortunately, while increasing cycling (at 100th cycle), the specific capacitance is decreased to 16 F g^{-1}. This may be due to the phase transition, unstable electrode and electrolyte layer and unwanted side reactions [21]. After 1000 cycles, Li-ion HSC cell lost its 84.45% of initial specific capacitance (14 F g^{-1}). On the other hand the Li-ion HSC cell fabricated using carbon coated $LiCo_{1/3}Ni_{1/3}Mn_{1/3}O_2$ provides improved as well as high stable cycling performance. Fig. 8 (d) shows the corresponding GCD curve of the fabricated cells. Initially, the cell provides a specific capacitance of 22 F g^{-1} and subsequently it increased to 60 F g^{-1} after 3000 cycles due to the activation effect [38], and it retains 56 F g^{-1} over 5000 cycles. The reason for this increasing capacitance is, the contribution of active materials is less at initial cycles due to the slow penetration of electrolyte. But the subsequent cycles, all the active sites are participating in the reaction, which in turn enhanced capacitance. Beyond activation process, the carbon coating on $LiCo_{1/3}Ni_{1/3}Mn_{1/3}O_2$ also enhances the specific capacitance due to adsorption/desorption of ions on the outer surface [59]. The coated amorphous carbon has some porous nature which provides a large electro-active surface area and shorter diffusion length for ionic conduction [67]. The battery type material into the carbonaceous network helps to enhance the diffusion and electron transfer limitations [38]. Fig. 8(e) shows the cycling stability curve of the fabricated hybrid cells using pristine $LiCo_{1/3}Ni_{1/3}Mn_{1/3}O_2$ and carbon coated $LiCo_{1/3}Ni_{1/3}Mn_{1/3}O_2$ as positive electrodes. After 1000 cycles, the specific capacitance of $LiCo_{1/3}Ni_{1/3}Mn_{1/3}O_2$||AC hybrid cell is decreased from 90 to 14 F g^{-1}. On the other hand, $LiCo_{1/3}Ni_{1/3}Mn_{1/3}O_2$@C||AC hybrid cell provides an increased specific capacitance from 22 to 56 F g^{-1} even after 5000 cycles. The interconnected carbon composite tightly connected with the metal oxides which can enhance the electronic conductivity, suppress the volume change and agglomeration of the active particles during the lithium ion insertion/de-insertion process [66]. The reason for increasing the specific capacitance of $LiCo_{1/3}Ni_{1/3}Mn_{1/3}O_2$@C composite is that the theoretical specific capacity of carbon (360 mAh g^{-1}) is higher than the $LiCo_{1/3}Ni_{1/3}Mn_{1/3}O_2$ (278 mAh g^{-1}) [59]. The carbon composite have some porous nature (Fig. 2d, e & f), which provides large electro-active surface area and shorter diffusion length for ionic conduction [67]. The activation and synergistic effect both contribute to higher specific capacitance of the Li ion HSC cell [38,68]. The calculated energy density and power density is 20 Wh kg^{-1} and 264 W kg^{-1}, respectively. Overall,

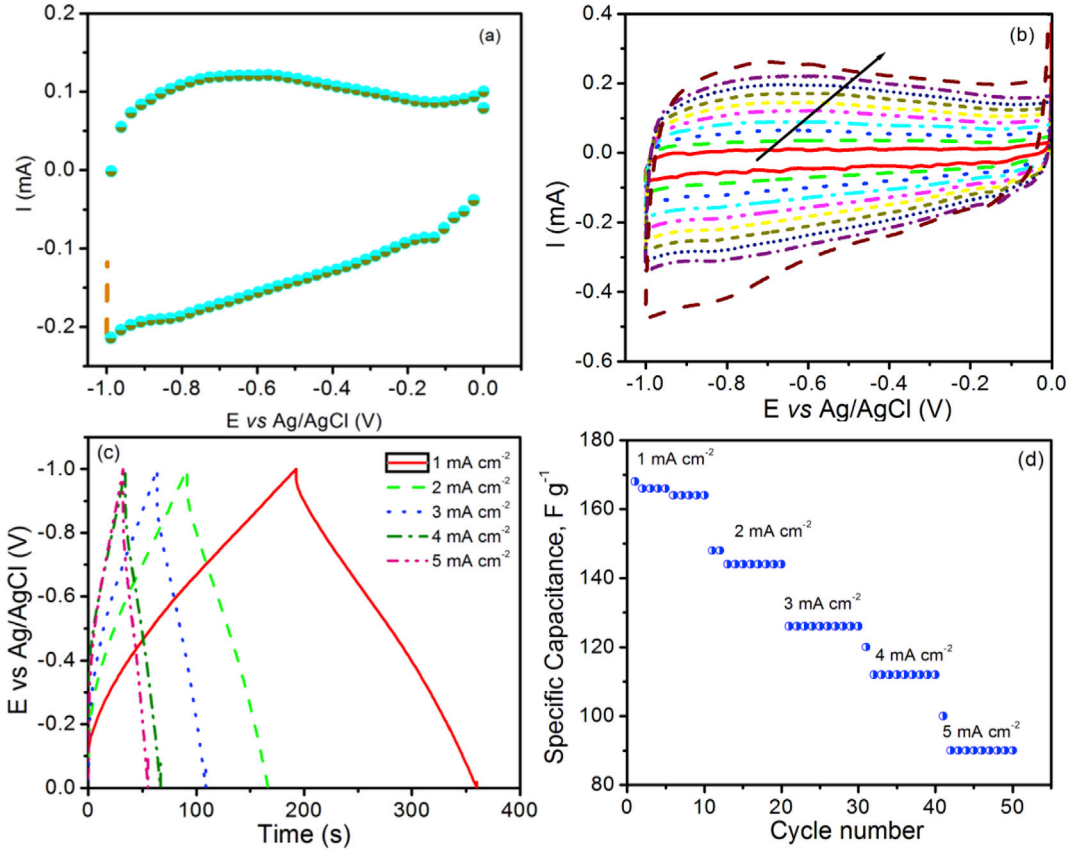

Fig. 7. CV curve of AC at (a) 0.5 mV s^{-1} and (b) at different scan rates from 0.1 to 1 mV s^{-1} (0.1 mV s^{-1} interval), (c) GCD curve at different current densities and (d) cyclic stability.

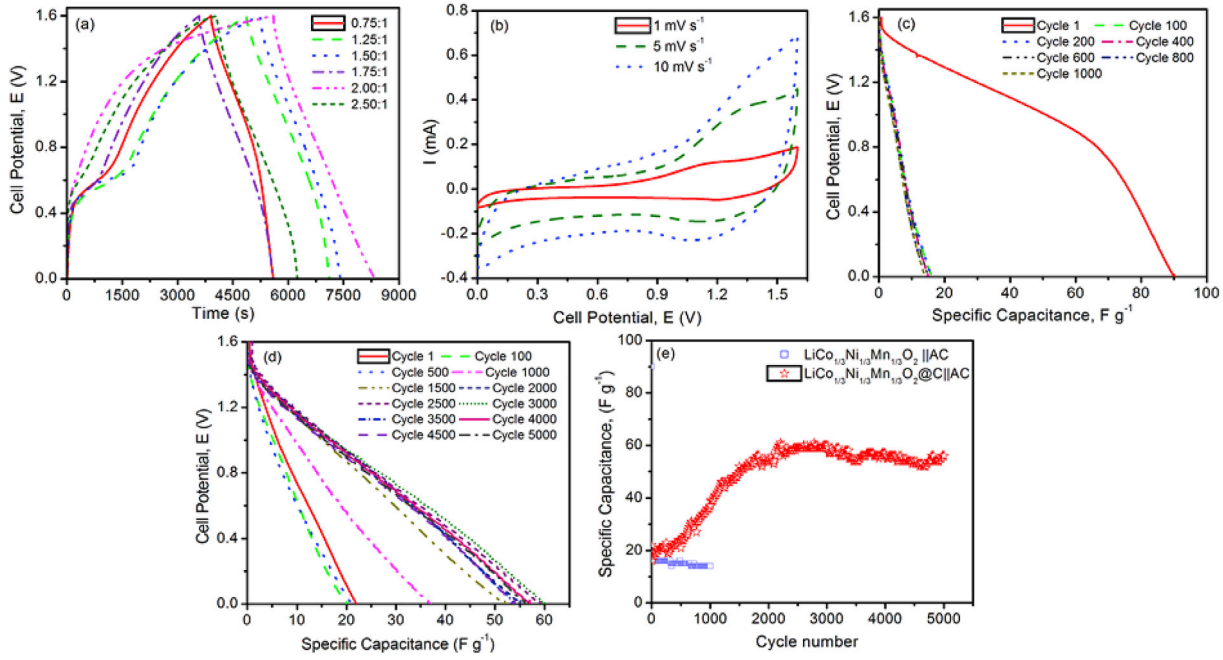

Fig. 8. (a) GCD curves of Li-HSC at different mass ratio, (b) CV curve of carbon coated $LiCo_{1/3}Ni_{1/3}Mn_{1/3}O_2$||AC hybrid cell at different scan rates, galvanostatic discharge curve of (c) $LiCo_{1/3}Ni_{1/3}Mn_{1/3}O_2$||AC and (d) carbon coated $LiCo_{1/3}Ni_{1/3}Mn_{1/3}O_2$||AC hybrid cells at 1 mA cm^{-2} with difference cycles and (e) Cycling stability curve of both cells.

the fabricated Li-HSC is more favour for long cycle applications. However, still it has the scope to improve the overall electrochemical performances especially, the rate capability of the $LiCo_{1/3}Ni_{1/3}Mn_{1/3}O_2$ electrode, specific capacitance of the cell, etc. by the following ways. (i) By improving the electrolyte concentration (saturated, 1 M, 2 M, etc.) since, at low concentration the high polarization created between cell and lithium sulphate electrolyte solution due to re-crystallization process of Li_2SO_4 crystals in the electrolyte solution upon slow evaporation of

water molecules [69]. (ii) To increase the electrode reactivity, tuning the structure of $LiCo_{1/3}Ni_{1/3}Mn_{1/3}O_2$ is mandatory particularly, the plane ($I_{(003)}/I_{(104)}$) ratio should be more than one [70]. (iii) The oxygen level in the electrolyte (normally 21%) can be reduced by N_2 treatment during electrochemical reactions, may improve the performance of the cells [71].

4. Conclusions

$LiCo_{1/3}Ni_{1/3}Mn_{1/3}O_2$ and activated carbon from *Agave Americana* is successfully synthesized through polymeric precursor method and chemical activation method. The structural analysis revealed that hexagonal α-$NaFeO_2$ crystal structure and prepared activated carbon belongs to turbostatic carbon structure. The morphological analysis assured that $LiCo_{1/3}Ni_{1/3}Mn_{1/3}O_2$ exhibits the non uniform shape particles and shows the presence of carbon clouds around the $LiCo_{1/3}Ni_{1/3}Mn_{1/3}O_2$ particles. The carbon coated $LiCo_{1/3}Ni_{1/3}Mn_{1/3}O_2$ half cell delivers the high specific capacitance of 30 mAh g^{-1} at 3 mA g^{-1} compared to pristine $LiCo_{1/3}Ni_{1/3}Mn_{1/3}O_2$ and activated carbon electrode delivers 126 F g^{-1} at 3 mA g^{-1}. The Li-ion HSC is fabricated using $LiCo_{1/3}Ni_{1/3}Mn_{1/3}O_2$ as a positive electrode and bio mass derived activated carbon as a negative electrode delivered 90 F g^{-1} and it could retain only 14 F g^{-1} even after 1000 cycles. However, Li-ion HSC using carbon coated $LiCo_{1/3}Ni_{1/3}Mn_{1/3}O_2$ delivered higher discharge capacity of 56 F g^{-1} and retained after 5000 cycles at current density of 1 mA cm^{-2}. The carbon composite on the positive electrode enhances the conductive network and it acted as a buffer layer to accommodate the stress induced by the lithium insertion/extraction. Finally, the fabricated Li-ion HSC cell exhibited energy density of 20 Wh kg^{-1} and power density of 264 W kg^{-1} with an output voltage of 1.6 V. The carbon composite with the positive electrode material facilitate to enhance the cycling stability and power density of the Li-HSC making it as a promising positive electrode material for Li-ion hybrid supercapacitor.

Acknowledgement

This work was supported by the National Research Foundation of Korea grant funded by the Korea government (Ministry of Science, ICT and Future Planning) (No. 2016R1A4A1012224).

References

[1] Y. Ma, H. Chang, M. Zhang, Y. Chen, Graphene-based materials for lithium-ion hybrid supercapacitors, Adv. Mater 27 (2015) 5296–5308.
[2] C.J. Hung, P. Lin, T.Y. Tseng, High energy density asymmetric pseudocapacitors fabricated by graphene/carbon nanotube/MnO_2 plus carbon nanotubes nanocomposite electrode, J. Power Sources 259 (2014) 145–153.
[3] S.M. Chen, R. Ramachandran, V. Mani, R. Saraswathi, Recent advancements in electrode materials for the high performance electrochemical supercapacitors: a review, Int. J. Electrochem. Sci. 9 (2014) 4072–4085.
[4] R. Aswathy, T. Kesavan, K.T. Kumaran, P. Ragupathy, Octahedral high voltage $LiNi_{0.5}Mn_{1.5}O_4$ spinel cathode: enhanced capacity retention of hybrid aqueous capacitors with nitrogen doped graphene, J. Mater. Chem. A 3 (2015) 12386–12395.
[5] C. Guan, W. Zhao, Y. Hu, Z. Lai, X. Li, S. Sun, H. Zhang, A.K. Cheetham, J. Wang, Cobalt oxide and N-doped Carbon nanosheets derived from a single two-dimensional metal-organic framework precursor and their application in flexible asymmetric Supercapacitors, Nanoscale Horiz. 2 (2017) 99–105.
[6] H. Kim, K.Y. Park, M.Y. Cho, M.H. Kim, J. Hong, S.K. Jung, K.C. Roh, K. Kang, High-performance hybrid supercapacitors based on graphene-wrapped $Li_4Ti_5O_{12}$ and activated carbon, ChemElectroChem 1 (2014) 125–130.
[7] J. Jiang, G. Tan, S. Peng, D. Qian, J. Liu, D. Luo, Y. Liu, Electrochemical performance of carbon-coated $Li_3V_2(PO_4)_3$ as a cathode material for asymmetric hybrid capacitors, Electrochim. Acta 107 (2013) 59–65.
[8] G.J. Wang, Q.T. Qu, B. Wang, Y. Shi, S. Tian, Y.P. Wu, R. Holze, Electrochemical intercalation of lithium ions into LiV_3O_8in an aqueous electrolyte, J. Power Sources 189 (2009) 503–506.
[9] H.B. Wang, K.L. Huang, Y.Q. Zeng, S. Yang, L.Q. Chen, Electrochemical properties of TiP_2O_7 and $LiTi(PO_4)_3$ as anode material for lithium ion battery with aqueous solution electrolyte, Electrochim. Acta 52 (2007) 3280–3285.
[10] M. Minakshi, P. Singha, D. Appadoo, D.E. Martin, Synthesis and characterization of olivine $LiNiPO_4$ for aqueous rechargeable battery, Electrochim. Acta 56 (2011) 4356–4360.
[11] M.S. Wu, M.J. Wang, J.J. Jow, W.D. Yang, C.Y. Hsieh, H.M. Tsai, Electrochemical fabrication of anatase TiO_2 nanostructure as an anode material for aqueous lithium-ion batteries, J. Power Sources 185 (2008) 1420–1424.
[12] P. He, J.L. Liu, W.J. Cui, J.Y. Luo, Y.Y. Xia, Investigation on capacity fading of $LiFePO_4$ in aqueous electrolyte, Electrochim. Acta 56 (2011) 2351–2357.
[13] A.B. Dighe, D.P. Dubal, R. Holze, Z. Anorg, Screen printed asymmetric supercapacitors based on $LiCoO_2$ and graphene oxide, Allg. Chem. 640 (2014) 2852–2857.
[14] Y.G. Wang, Y.Y. Xia, A new concept hybrid electrochemical supercapacitor: carbon/$LiMn_2O_4$ aqueous system, Electrochem. Commun. 7 (2005) 1138–1142.
[15] A.D. Pasquier, I. Plitz, J. Gural, F. Badway, G.G. Amatucci, Power-ion battery: bridging the gap between Li-ion and supercapacitor chemistries, J. Power Sources 136 (2004) 160–170.
[16] A. Mahmoud, I. Saadoune, J.M. Amarilla, R. Hakkou, On the $LiCo_{2/3}Ni_{1/6}Mn_{1/6}O_2$ positive electrode material, Electrochim. Acta 56 (2011) 4081–4086.
[17] N. Nitta, F. Wu, J.T. Lee, G. Yushin, Li-ion battery materials: present and future, Mater. Today 18 (2015) 252–264.
[18] K.S. Lee, S.T. Myung, K. Amine, H. Yashiro, Y.K. Sun, Structural and electrochemical properties of layered $Li[Ni_{1-2x}Co_xMn_x]O_2$ (x=0.1-0.3) positive electrode materials for Li-Ion batteries, J. Electrochem Soc. 154 (2007) A971–A977.
[19] P. He, H. Yu, D. Li, H. Zhou, Layered lithium transition metal oxide cathodes towards high energy lithium-ion batteries, J. Mater. Chem. 22 (2012) 3680–3695.
[20] J.R. Dahn, Y.D. Wang, J.W. Jiang, The reactivity of delithiated $Li(Ni_{1/3}Co_{1/3}Mn_{1/3})O_2$, $Li(Ni_{0.8}Co_{0.15}Al_{0.05})O_2$ of $LiCoO_2$ with non-aqueous electrolyte, Electrochem Commun. 9 (2007) 2534–2540.
[21] Y. Zhao, Y.Y. Wang, Q.Y. Lai, L.M. Chen, Y.J. Hao, X.Y. Ji, Pseudo capacitance properties of AC/$LiNi_{1/3}Co_{1/3}Mn_{1/3}O_2$ asymmetric supercapacitor in aqueous electrolyte, Synth. Met. 159 (2009) 331–337.
[22] Y.G. Wang, J.Y. Luo, C.X. Wang, Y.Y. Xia, Hybrid aqueous energy storage cells using Activated Carbon and Lithium-ion intercalated compounds II. Comparison of $LiMn_2O_4$, $LiCo_{1/3}Ni_{1/3}Mn_{1/3}O_2$ and $LiCoO_2$ positive electrodes, J. Electrochem. Soc. 153 (2006) A1425–A1431.
[23] P.R. Ilango, T. Subburaj, K. Prasanna, Y.N. Jo, C.W. Lee, Physical and electrochemical performance of $LiNi_{1/3}Co_{1/3}Mn_{1/3}O_2$ cathodes coated by Sb_2O_3 using a sol-gel process, Mater. Chem. Phys. 158 (2015) 45–51.
[24] J. Huang, Z. Yang, X. Xie, Z. Feng, Z. Zhang, Preparation of cribriform sheet-like carbon-coated Zinc oxide with improved electrochemical performance, J. Power Sources 289 (2015) 8–16.
[25] J. Sun, Y. Sun, L. Gai, H. Jiang, Y. Tian, Carbon-coated mesoporous $LiTi_2(PO_4)_3$ nanocrystals with superior performance for lithium-ion batteries, Electrochim. Acta 200 (2016) 66–74.
[26] A. Suryawanshi, M. Biswal, D. Mhamane, P. Yadav, A. Banerjee, P. Yadav, S. Patil, V. Aravindan, S. Madhavi, S. Ogale, A comparative evaluation of differently synthesized high surface area carbons for Li-ion hybrid electrochemical supercapacitor application: pore size distribution holds the key, Appl. Mater. Today 2 (2016) 1–6.
[27] C. Guan, X. Liu, W. Ren, X. Li, C. Cheng, J. Wang, Rational design of metal-organic framework derived hollow $NiCo_2O_4$ arrays for flexible supercapacitor and electrocatalysis, Adv. Energy Mater 1602391 (2017) 1–8.
[28] S.T. Senthilkumar, R. Kalai Selvan, Flexible fiber supercapacitor using biowaste-derive porous carbon, ChemElectroChem 2 (2015) 1111–1116.
[29] S.T. Senthilkumar, R. Kalaiselvan, Y.S. Lee, J.S. Melo, Electric double layer capacitor and its improved specific capacitance using redox additive electrolyte, J. Mater. Chem. A 1 (2013) 1086–1095.
[30] S.T. Senthilkumar, B. Senthilkumar, S. Balaji, C. Sanjeeviraja, R. Kalai Selvan, Preparation of activated carbon from sorghum pith and its structural and electrochemical properties, Mater. Res. Bull. 46 (2011) 413–419.
[31] A. Hulle, P. Kadole, P. Katkar, Agave americana leaf fibers, Fibers 3 (2015) 64–75.
[32] G.J. Wang, L.J. Fu, N.H. Zhao, Y.P. Wu, R. Holze, An aqueous rechargeable lithium battery based on LiV_3O_8 and $Li[Ni_{1/3}Co_{1/3}Mn_{1/3}O_2]O_2$, J. Appl. Electrochem 38 (2008) 579–581.
[33] A.A. Titov, Z.V. Eremenko, E.G. Goryacheva, N.P. Sokolova, N.L. Opolchenova, N.N. Stepareva, G.P. Korobko, Synthesis, structure and some properties of $LiNi_{1/3}Co_{1/3}Mn_{1/3}O_2$, Inorg. Mater 49 (2013) 202–208.
[34] S.K. Kim, W.T. Jeong, H.K. Lee, J. Shim, Characteristics of $LiNi_{1/3}Co_{1/3}Mn_{1/3}O_2$ cathode powder prepared by different method in lithium rechargeable batteries, Int. J. Electrochem. Sci. 3 (2008) 1504–1511.
[35] A.M. Hashem, R.S. El-Tawil, M. Abutabi, A.E. Eid, Pristine and coated $LiNi_{1/3}Mn_{1/3}Co_{1/3}O_2$ as positive electrode materials for Li-ion batteries, Res. Eng. Struct. Mat 1 (2015) 81–97.
[36] L.A. Riley, S.V. Atta, A.S. Cavanagh, Y. Yan, S.M. George, P. Liu, A.C. Dillon, S.-H. Lee, Electrochemical effects of ALD surface modification on combustion synthesized $LiNi_{1/3}Mn_{1/3}Co_{1/3}O_2$ as a layered-cathode material, J. Power Sources 196 (2011) 3317–3324.
[37] H. Bae, T. Ahmad, I. Rhee, Y. Chang, S.U. Jin, S. Hong, Carbon-coated iron oxide nanoparticles as contrast agents in magnetic resonance imaging, Nanoscale Res. Lett. 7 (2012) 1–5.
[38] S. Balasubramanian, K.K. Purushothaman, Carbon coated flowery V_2O_5 nanostructure as novel electrode material for high performance supercapacitors, Electrochim. Acta 186 (2015) 285–291.
[39] K. Song, Y. Lee, M.R. Jo, K.M. Nam, Y.M. Kang, Comprehensive design of carbon-encapsulated Fe_3O_4 nanocrystals and their lithium storage properties, Nanotechnology 23 (2012) 1–6.
[40] D.P. Cong, J.H. Kim, S.Y. Jeong, J.H. Choi, J. Kim, C.R. Cho, Enhanced electrochemical performance of carbon-coated TiO_2 nanobarbed fibers as anode material for lithium-ion batteries, Electrochem. Commun. 60 (2015) 204–207.

[41] J. Pan, Y. Wen, J. Cheng, S. Bai, J. Pan, G. Cao, Y. Yang, Effects of various electrolytes on the electrochemical performance of spinel $LiMn_2O_4$ in aqueous solutions, Int. J. Electrochem Sci. 10 (2015) 9324–9332.
[42] C. Punckt, M.A. Pope, J. Liu, Y. Lin, I.A. Aksay, Electrochemical performance of Graphene as effected by electrode porosity and graphene functionalization, Electroanal 22 (2010) 2834–2841.
[43] Y. Gong, D. Li, Q. Fu, C. Pan, Influence of graphene microstructures on electrochemical performance for supercapacitors, Prog. Nat. Sci. Mater. Int. 25 (2015) 379–385.
[44] Q.T. Qu, B. Wang, L.C. Yang, Y. Shi, S. Tian, Y.P. Wu, Study on electrochemical performance of activated carbon in aqueous Li_2SO_4, Na_2SO_4 and K_2SO_4 electrolytes, Electrochem. Commun. 10 (2008) 1652–1655.
[45] X. Gu, J.L. Liu, J.H. Yang, H.J. Xiang, X.G. Gong, Y.Y. Xia, First-principles study of H^+ intercalation in layer-structured $LiCoO_2$, J. Phys. Chem. C 115 (2011) 12672–12676.
[46] M.M. Rao, M. Jayalakshmi, O. Schaf, U. Guth, H. Wulff, F. Scholz, Electrochemical behavior of solid lithium nickelate ($LiNO_2$) in an aqueous electrolyte system, J. Solid State Electrochem 4 (1999) 17–23.
[47] G. Wang, L. Fu, N. Zhao, L. Yang, Y. Wu, H. Wu, An aqueous rechargeable lithium battery with good cycling performance, Chem. Int. Ed. 46 (2007) 295–297.
[48] N.N. Sinha, P. Ragupathy, H.N. Vasan, N. Munichandraiah, Electrochemical characterization of submicron size particles of $LiMn_2O_4$ in aqueous electrolytes, Int. J. Electrochem. Sci. 3 (2008) 691–710.
[49] V. Aravindan, M. Reddy, S. Madhavi, G. Rao, B. Chowdari, Electrochemical performance of α-MnO_2 nanorods/activated carbon hybrid supercapacitor, Nanosci. Tech. Lett. 4 (2012) 724–728.
[50] F. Wang, S. Xiao, Z. Chang, Y. Yang, Y. Wu, Nanoporous $LiNi_{1/3}Co_{1/3}Mn_{1/3}O_2$ as an ultra-fast charge cathode material for aqueous rechargeable lithium batteries, Chem. Commun. 49 (2013) 9209–9211.
[51] M. Takahashi, S.I. Tobishima, K. Takei, Y. Sakurai, Reaction behavior of $LiFePO_4$ as a cathode material for rechargeable lithium batteries, Solid State Ionics 148 (2002) 283–289.
[52] S. Franger, C. Bourbon, F. LeCras, Optimized lithium iron phosphates for high-rate electrochemical applications, J. Electrochem. Soc. 151 (2004) A1024–A1027.
[53] D.Y.W. Yu, C. Fietzek, W. Weydanz, K. Donoue, T. Inoue, H. Kurokawa, S. Fujitani, Study of $LiFePO_4$ by cyclic voltammetry, J. Electochem. Soc. 154 (2007) A253–A257.
[54] X.H. Rui, N. Ding, J. Liu, C. Li, C.H. Chen, Analysis of the chemical diffusion coefficient of lithium ions in $Li_3V_2(PO_4)_3$ cathode material, Electrochim. Acta 55 (2010) 2384–2390.
[55] Y. Shi, L. Wen, F. Li, H.–M. Cheng, Nanosized $Li_4Ti_5O_{12}$/graphene hybrid materials with low polarization for high rate lithium ion batteries, J. Power Sources 196 (2011) 8610–8617.
[56] B.K. Zou, H.Y. Wang, Z.Y. Qiang, Y. Shao, X. Sun, Z.Y. Wen, C.H. Chen, Mixed-carbon-coated $LiMn_{0.4}Fe_{0.6}PO_4$ nanopowders with excellent high rate and low temperature performances for lithium-ion batteries, Electrochim. Acta 196 (2016) 377–385.
[57] K. Zaghib, J.G. Goodenough, A. Mauger, C. Julien, Unsupported claims of ultrafast charging of $LiFePO_4$ Li-ion batteries, J. Power Sources 194 (2009) 1021–1023.
[58] J.B. Goodenough, Y. Kim, Challenges of rechargeable batteries, Chem. Mater 22 (2010) 587–603.
[59] R. Sathish, V. Aravindan, W.C. Ling, S. Madhavi, Carbon-coated $Li_3V_2(PO_4)_3$ as insertion type electrode for lithium-ion hybrid electrochemical capacitors: an evaluation of anode and cathodic performance, J. Power Sources 281 (2015) 310–317.
[60] H.H. Lim, I.C. Jang, S.B. Lee, K. Karthikeyan, V. Aravindan, Y.S. Lee, The important role of adipic acid on the synthesis of nanocrystalline lithium iron phosphate with high rate performance, J. Alloys Compd. 495 (2010) 181–184.
[61] V. Aravindan, K. Karthikeyan, K.S. Kang, W.S. Yoon, W.S. Kim, Y.S. Lee, Influence of carbon towards improved lithium storage properties of Li_2MnSiO_4 cathodes, J. Mater. Chem. 21 (2011) 2470–2475.
[62] Y. Liu, J.S. Xue, T. Zheng, Mechanism of lithium insertion in hard carbons prepared by pyrolysis of epoxy resins, Carbon 34 (1996) 193–200.
[63] E.J. Lee, Y.J. Lee, J.K. Kim, M. Lee, J. Yi, J.R. Yoon, J.C. Song, J.K. Song, Oxygen group-containing activated carbon aerogel as an electrode material for supercapacitor, Mat. Res. Bull. 70 (2015) 209–214.
[64] K. Vijaya Sankar, S.T. Senthil Kumar, L. John Berchmans, C. Sanjeeviraja, R. Kalai Selvan, Effect of reaction time on the synthesis and electrochemical properties of Mn_3O_4 nanoparticles by microwave assisted reflux method, Appl. Surf. Sci. 259 (2012) 624–630.
[65] R. Satish, V. Aravindan, W.C. Ling, N.K. Woei, S. Madhavi, Macroporous carbon from human hair: a journey towards the fabrication of high energy Li-ion capacitors, Electrochim. Acta 182 (2015) 474–481.
[66] X. Chai, C. Shi, E. Lui, J. Li, N. Zhao, C. He, Hierarchically structured carbon-coated SnO_2-Fe_3O_4 microparticles with enhanced lithium storage performance, Appl. Surf. Sci. 361 (2016) 1–10.
[67] N.B. Trung, T.V. Tam, D.K. Dang, K.F. Babu, E.J. Kim, J. Kim, W.M. Choi, Facile synthesis of three-dimensional graphene/nickel oxide nanoparticles composites for high performance supercapacitor electrodes, Chem. Eng. J. 264 (2015) 603–609.
[68] A. Borenstein, O. Hanna, R. Attias, S. Luski, T. Brousse, D. Aurbach, Carbon-based composite materials for supercapacitor electrodes: a review, J. Mater Chem. A 5 (2017) 12653–12672.
[69] A. Ramanujapuram, D. Gordon, A. Magasinski, B. Ward, N. Nitta, C. Huang, G. Yushin, Degradation and stabilization of lithium cobalt oxide in aqueous electrolytes, Energy Environ. Sci. 9 (2016) 1841–1848.
[70] R. Zhao, Z. Yang, J. Chen, Z. Chen, J. Liang, H. Chen, Novel solvo/hydrothermal assisted co-precipitation method for facted LiNi1/3Mn1/3Co1/3O2 cathode material, J. Alloys Compd. 627 (2015) 206–210.
[71] H. Kim, J. Hong, K.Y. Park, H. Kim, S.W. Kim, K. Kong, Aqueous rechargeable Li and Na ion batteries, Chem. Rev. 114 (2014) 11788–11827.